Small

NANO · MICRO small
www.small-journal.com

RESEARCH ARTICLE OPEN ACCESS

Topography-Free Dual-Lubricant Patterned Slippery Surfaces for Programmable Droplet Control and High-Performance Water Harvesting

Jinchul Yang[1] | Eonji Kim[1,2] | Doo Young Choi[3] | Jineun Lee[4] | Hwanhui Yun[1] | Jinhee Lee[1] | Kyuyoung Heo[1] | In Hwan Jung[2] | Yong-Jae Jin[5] | Joon Heon Kim[6] | Giseop Kwak[4] | Wang-Eun Lee[1]

[1]Reliability Assessment Center for Chemical Materials, Korea Research Institute of Chemical Technology (KRICT), Daejeon, Republic of Korea | [2]Department of Organic and Nano Engineering, and Human-Tech Convergence Program, Hanyang University, Seoul, Republic of Korea | [3]Department of Biomedical Sciences, School of Medicine, Kyungpook National University, Daegu, Republic of Korea | [4]Department of Polymer Science and Engineering, Polymeric Nanomaterials Laboratory, Kyungpook National University, Daegu, Republic of Korea | [5]Department of Specialty Chemicals, Division of Specialty and Bio-based Chemicals Technology, Korea Research Institute of Chemical Technology (KRICT), Ulsan, Republic of Korea | [6]Advanced Photonics Research Institute, Gwangju Institute of Science and Technology, Gwangju, Republic of Korea

Correspondence: Joon Heon Kim (joonhkim@gist.ac.kr) | Giseop Kwak (gkwak@knu.ac.kr) | Wang-Eun Lee (welee@krict.re.kr)

Received: 4 September 2025 | **Revised:** 30 December 2025 | **Accepted:** 26 January 2026

Keywords: conjugated polymer | dual-lubricant patterning | programmable droplet control | slippery liquid-infused surfaces | sustainable water condensation surfaces

ABSTRACT

Passive droplet control is critical for next-generation water harvesting, fluidic logic, and adaptive wetting surfaces. Here, we report a scalable, topography-free slippery liquid-infused porous surface (SLIPS) based on poly[1-phenyl-2-[p-(trimethylsilyl)phenyl]acetylene] (PTMSDPA). By selectively chemically fluorinating specific regions of the porous PTMSDPA film, followed by sequential infusion of two immiscible hydrophobic lubricants into their respective affinity-matched polymer matrices, this approach enables interfacial energy contrasts that direct droplet motion. The heterogeneous oil-infused porous surface (HOIPS) has a unique intrinsic fluorescence enabling real-time, dye-free visualization of infiltrated lubricant domains. Owing to its ultrathin (~200 nm) and flexible polymer structure, the HOIPS enables controllable droplet motion on flat, flexible, and curved substrates without reliance on surface topography, physical confinement, or asymmetric geometries. Sub-millimeter-scale HOIPS line patterns enable controlled droplet coalescence, shedding diameter, and release timing during condensation, and optimized patterns exhibit up to 2.5× higher water-harvesting performance compared to fluorinated-oil-based SLIPS, providing a material-efficient strategy for liquid-repellent surfaces. Taken together, these results establish PTMSDPA-based HOIPS as a versatile platform for controlled droplet manipulation and condensation management.

1 | Introduction

Liquid-repellent surfaces have garnered significant interest in both academia and industry due to their unique interfacial properties [1]. Barthlott et al. reported in 1997 the water-repellent and self-cleaning properties of plant surfaces, a phenomenon now widely known as the lotus effect [2]. The lotus leaf surface features hierarchical micro-bumps covered with nanoscale hydrophobic epicuticular waxes, preventing the adhesion of water droplets and other contaminants on the leaf surface. Since this concept was established, synthetic approaches inspired by the lotus effect have been extensively explored, relying on stable air–liquid

interfaces to achieve superhydrophobicity [3–5]. As a different approach inspired by the Nepenthes pitcher plant, Wong et al. proposed the concept of slippery liquid-infused porous surfaces (SLIPSs), repelling test liquids by infusing a lubricant into a micro-/nanotextured substrate [6]. When the infused lubricant fully wets and stably adheres to the substrate, preferentially wets the solid over the test liquid, and remains immiscible with the test liquid, SLIPSs enable self-healability, pressure stability, low contact-angle hysteresis, and excellent omniphobicity.

Liquid-repellent properties can be adjusted by tuning the physicochemical characteristics of various solid substrates and by selecting appropriate lubricant types. Accordingly, subsequent developments have explored a variety of solid matrices, including fluorocarbon derivatives [7–9], polydimethylsiloxane (PDMS) [10–12], polystyrene-*b*-polylactide [13], poly(ethyleneimine)/poly(vinyl-4,4-dimethylazlactone) (PEI/PVDMA) multilayers [14], and polyorganosilazane [15] for tailoring SLIPS performance. Manna et al. fabricated lubricant-infused nanoporous PEI/PVDMA multilayers with interfacial properties that could be tuned to manipulate the behavior of fluids in contact with the surface [14]. Although spatially patterned porous multilayers with sticky spots show potential for controlling the sliding direction of aqueous droplets, detailed insights remain to be further explored. In line with this trend, SLIPSs have increasingly been explored for achieving directional droplet manipulation.

The directional motion control of water droplets based on SLIPSs has drawn considerable attention in the fields of water collection [16–21], microfluidic devices [22–25], droplet microarray [26], and gas collection [27]. Generally, the directional motion of droplets on a slippery surface can be manipulated by controlling its topology. Inspired by the bumpy surface geometry of beetles, Park et al. used slippery asymmetric bumps to guide droplet motion in the widening-slope direction under the action of capillary forces regardless of the gravitational force [16]. The directional transport of droplets on slippery surfaces can be governed either by engineering surface topography [16, 28–30] or by incorporating hydrophilic micropatterns into SLIPSs [17, 20, 31], enabling anisotropic wettability and guided droplet motion. Yang et al. designed anisotropic 3D topological SLIPSs based on the Wenzel state [28]. These nanotextured SLIPSs incorporated wedge-shaped structures and enabled self-driven droplet transport based on the Laplace pressure gradient. Kamei et al. prepared an omniphobic SLIPS film with hybrid honeycomb and pincushion-like porous structures [29], realizing directional droplet motion toward the honeycomb surface based on adhesion force differences driven by surface topography. Recent studies have explored directional droplet manipulation through chemical patterning of surfaces with two immiscible lubricants [32, 33]. Pelizzari et al. demonstrated capillarity-based droplet propulsion across dual-lubricant interfaces [32], eliminating the need for topography. While this study elegantly demonstrated droplet self-propulsion on SLIPS using photolithographically defined chemical patterns, the distinction between the two lubricant domains relied on fluorescent dye infusion into the lubricants, and the demonstrations were primarily conducted on rigid, planar substrates. Consequently, the extension of such patterning strategies to mechanical compliant or highly curved substrates was not the central focus of that work. Furthermore, although the study provided an insightful proof-of-concept, its applicability to practical droplet-driven processes, such as water harvesting or condensation management, was not explicitly addressed.

Here, we present a flexible, topography-free SLIPS platform based on chemically patterned lubricant-infused porous poly[1-phenyl-2-[p-(trimethylsilyl)phenyl]acetylene] (PTMSDPA) films. This semi-flexible, ultrahigh-molecular-weight polymer exhibits high dimensional stability when swollen in diverse fluidic oils, a result of its high fractional free volume and glassy nature [34]. In addition, PTMSDPA enables independent wetting and robust adhesion of two immiscible lubricants on chemically heterogeneous surfaces, which is achieved through nano/micro-scale patterning and selective surface modification and is supported by its favorable mechanical properties and chemical/thermal stability [35]. This platform offers three distinct advantages: (1) Fluorescence-based visualization without dyes: Intrinsic fluorescence enables direct, real-time monitoring of lubricant patterning—facilitating quality control across large areas. (2) Ultrathin and flexible substrate compatibility: ~200 nm thick PTMSDPA films enable robust operation under curvature and mechanical deformation. (3) Sustainable and high-performance water harvesting: The optimized dual-lubricant pattern delivers over 2.5 × higher water harvesting efficiency while using less than half the amount of fluorinated lubricant required by fully infused fluorinated-oil-infused porous surfaces (FOIPS), and enables tunable control of first-droplet release. In addition, simple geometric design rules based on various combinations of SiOIPS and FOIPS line widths were identified as key factors governing droplet coalescence, shedding diameter, and release timing during condensation. In benchmarking tests, the water-harvesting performance of our heterogeneous oil-infused porous surface (HOIPS) surpasses that of representative SLIPS designs reported in the literature, as detailed later in this work. Together, these attributes enable efficient dual-lubricant SLIPS design and programmable droplet behavior, providing a versatile platform for studying and implementing droplet manipulation and condensation control.

2 | Results and Discussion

2.1 | Slippery Liquid-Infused PTMSDPA Film

PTMSDPA (Figure 1a), a diphenylacetylene-based polymer with a high fractional free volume (0.26), exhibits swelling-induced emission enhancement (SIEE), which enables the detection of swelling induced by various fluids [34, 35]. Based on this property, we analyzed the swelling behaviors of PTMSDPA films infused with silicone (Si 5, Si 100, and Si 500 cSt), polyphenylmethylsiloxane (PPMS; Si AP100, Si AP1000, and Si AR), paraffin, jojoba, and mineral oils (Figures S1 and S2).

The infused PTMSDPA films exhibited notable SIEE, as evidenced by their increased fluorescence (FL) intensity ratio ($I_{swelling}/I_{dry}$). For the films infused with silicone oils, $I_{swelling}/I_{dry}$ increased from 4.6 ± 0.03 to 5.4 ± 0.47 with the increasing oil viscosity. The films infused with PPMS, paraffin, jojoba, and mineral oils exhibited markedly higher $I_{swelling}/I_{dry}$ ratios (7.0 ± 0.20 to 9.2 ± 0.27) indicating swelling effects. The $I_{swelling}/I_{dry}$ ratio was affected by the viscosity of the infused oil and its affinity for the film. However, the $I_{swelling}/I_{dry}$ value of a fluorinated oil

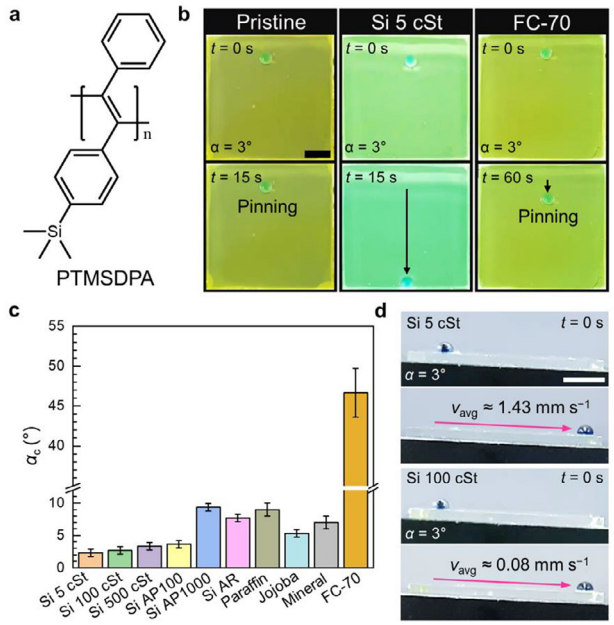

FIGURE 1 | (a) Chemical structure of poly[1-phenyl-2-[*p*-(trimethylsilyl)phenyl]acetylene] (PTMSDPA). (b) Fluorescence (FL) images illustrating the sliding movement of water droplets on the surface of oil-free and oil (Si 5 cSt and FC-70)-treated PTMSDPA films at a tilting angle (α) of 3°. Droplet volume = 5 μL, scale bar = 5 mm. (c) Critical water sliding angles (means ± standard deviations (SDs) for n = 3) on the surfaces of PTMSDPA films infused with various lubricants. (d) Photographs illustrating the sliding movement of water droplets on the surfaces of PTMSDPA films infused with Si 5 cSt and Si 100 cSt at α = 3°. Droplet volume = 5 μL, scale bar = 5 mm.

(FC-70)-infused film was as low as 1.9 ± 0.09, indicating an almost complete absence of swelling that was ascribed to the lack of efficient diffusion due to the low affinity of the fluorinated oil for the PTMSDPA film.

Figure 1b shows the sliding movement of 5-μL water droplets on the surfaces of oil-free and oil-infused PTMSDPA films at a tilting angle (α) of 3°. The water droplets were firmly pinned on the pristine surface and stopped after moving ~2 mm on the FC-70-infused surface. Conversely, easy sliding was observed on the Si 5 cSt-infused surface, with the force needed to move a droplet determined as ~5% (sin 3° = 0.052) of the gravity force acting thereon.

To identify lubricant types suitable for the fabrication of SLIPSs based on PTMSDPA, we determined critical sliding angles (α_c, defined as the α value at which a 5-μL water droplet moves by >20 mm, Video S1) for the surfaces of PTMSDPA films treated with different oils (Figure 1c). The α_c values were less than 10° for all oils except FC-70 and were lowest (2°–4°) for Si 5, 100, and 500 cSt, demonstrating the suitability of PTMSDPA as a SLIPS material compatible with a wide range of lubricants with the exception of fluorinated oils.

In particular, the surfaces infused with the silicone oils (Si 5, 100, and 500 cSt) were more slippery than those treated with the other oils. To verify the relationship between the sliding speed and viscosity, we observed droplet movement on the surfaces infused with the silicone oils (Figure 1d). The sliding speed of droplets on the Si 5 cSt-infused surface was ~17.8-fold higher than that on the Si 100 cSt-infused surface. On slippery surfaces, droplet sliding is driven by the gravitational force component ($mg\sin\alpha$), which is balanced by the surface dissipation force ($F \propto \eta U/h$, where η, U, and h represent the lubricant viscosity, droplet velocity, and thickness of lubricant film, respectively [36]. Therefore, a higher-viscosity lubricant (Si 100 cSt) results in a lower sliding velocity than Si 5 cSt. These observations suggest that lubricant viscosity is a critical parameter governing droplet transport on SLIPSs by the modulation of sliding dynamics.

2.2 | Porous Fluorinated PTMSDPA Film

To create a slippery surface by the stable wetting and adhesion of a fluorinated oil, a porous fluorinated PTMSDPA (F-PTMSDPA) film was fabricated via porosification and subsequent fluorination by plasma treatment and coating with trichloro(1*H*,1*H*,2*H*,2*H*-perfluorooctyl)silane (PFOTS) (Figure 2a). Because FC-70 does not appreciably swell fluorinated PTMSDPA, stable lubricant retention cannot rely solely on chemical affinity between the liquid and the solid substrate. Instead, effective retention requires a sufficiently large internal surface area provided by micro-/nanostructuring, which enables capillary anchoring and complete wetting of the fluorinated lubricant within the matrix.[6] Accordingly, nanoporous structures were introduced by employing polystyrene (PS) as a sacrificial polymer, exploiting the difference in solubility between PTMSDPA and PS in methyl ethyl ketone (MEK), followed by fluorination to achieve both physical anchoring and chemical affinity of the fluorinated lubricant. Figure S3 shows the field-emission scanning electron microscopy (FE-SEM) images of PTMSDPA after the removal of PS from PTMSDPA/PS blend films with different compositions. The film with a PTMSDPA:PS mass ratio of 0.4:0.6 exhibited porous micro-/nanotextures and a well-connected polymer matrix and was therefore suitable for SLIPS construction, as the incomplete wetting of the structurally defective polymer matrix could result in droplet pinning on the air-exposed surface [37].

The porous PTMSDPA and F-PTMSDPA films exhibited no notable structural differences, featuring measured thicknesses of 215 ± 9 and 210 ± 13 nm, respectively (Figure 2b). The fluorination of PTMSDPA was confirmed by Fourier-transform infrared (FT-IR) analysis (Figure 2c). The FT-IR spectrum of PTMSDPA exhibited peaks ascribed to the breathing vibration of the benzene ring and symmetric bending vibration of the Si—CH_3 moiety at ~1120 and 1245 cm^{-1}, respectively [38, 39]. After fluorination, strong and sharp absorption peaks emerged at ~1142 and 1188 cm^{-1}, corresponding to the deformation and stretching vibrations of C—F bonds, respectively [40].

The sliding behavior of the porous F-PTMSDPA film infused with FC-70 was further investigated at α = 3° (Figure 2d). The water droplet smoothly slid on the film, indicating its excellent water repellency due to the efficient fixation of the fluorine-containing lubricant. The absence of FL enhancement in the fluorinated region infused with FC-70 suggested that this oil infiltrated the

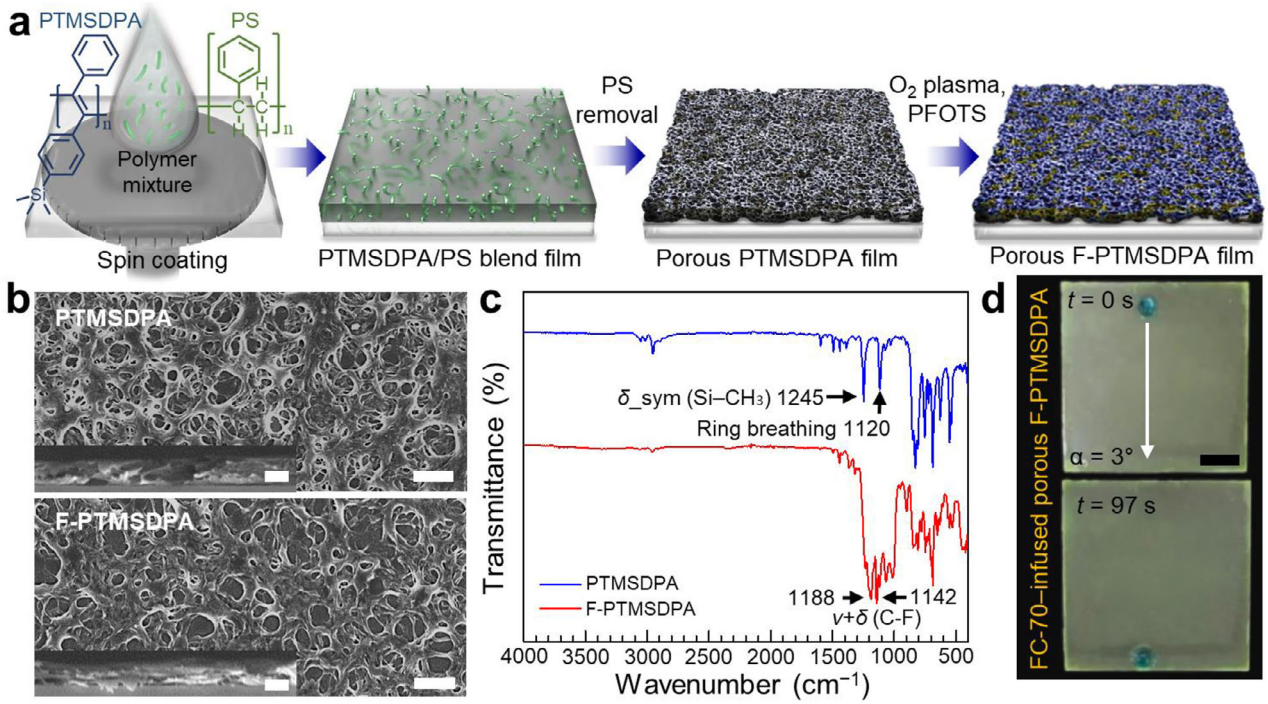

FIGURE 2 | (a) Schematic of porous PTMSDPA and fluorinated PTMSDPA (F-PTMSDPA) film fabrication. (b) Field-emission scanning electron microscopy images of porous PTMSDPA and F-PTMSDPA films prepared under optimized conditions at a PTMSDPA:polystyrene mass ratio of 0.4:0.6. The top-view and cross-sectional scale bars are 1 μm and 200 nm, respectively. (c) Fourier-transform infrared spectra of PTMSDPA and F-PTMSDPA films. (d) FL images depicting the sliding movement of water droplets on an FC-70-infused porous F-PTMSDPA film at $\alpha = 3°$. Droplet volume = 5 μL, scale bar = 5 mm.

porous structure without sufficiently swelling the polymer matrix to increase the intermolecular distance between the PTMSDPA chains.

To evaluate the stability of the lubricating films, we compared the total interfacial energies of three different configurations. Configuration A represents the state in which the solid polymeric film is completely wetted by water (Liquid A). Configuration 1 refers to Liquid A entirely suspended on a polymeric film fully wetted by the lubricant (Liquid B), while Configuration 2 refers to a polymeric film fully wetted by Liquid B (Figure S4). To ensure that the polymer film is preferentially wetted by the lubricant rather than water, the interfacial energy differences (ΔE_1 and ΔE_2) must satisfy the following equations (Equations (1) and (2)) derived from Young's equation [6]:

$$\Delta E_1 = R(\gamma_B \cos\theta_B - \gamma_A \cos\theta_A) - \gamma_{AB} > 0 \quad (1)$$

$$\Delta E_2 = R(\gamma_B \cos\theta_B - \gamma_A \cos\theta_A) + \gamma_A - \gamma_B > 0 \quad (2)$$

Here, E_1 and E_2 are the total interfacial energies per unit area for Configurations 1 and 2, respectively; R is the actual/projected solid area roughness ratio; γ_A and γ_B are the water and lubricant surface tensions, respectively; γ_{AB} is the interfacial tension between water and the lubricant; and θ_A and θ_B are the equilibrium contact angles of water and the lubricant on a flat solid surface, respectively. For most lubricants (including silicone, paraffin, jojoba, and mineral oils), ΔE_1 and ΔE_2 were positive, confirming the formation of a stable solid–liquid interface (Figures S5–S8 and Table S1). However, the ΔE_1 value for FC-70 was −10.4, explaining the unsuccessful realization of a slippery surface on untreated PTMSDPA films with FC-70, in contrast to most other lubricants (Figure 1c). The ΔE_1 and ΔE_2 values for the combination of F-PTMSDPA (solid), water (Liquid A), and FC-70 (Liquid B) were calculated as 4.8 and 114.5, respectively, demonstrating that the porous F-PTMSDPA surface could stably retain FC-70.

2.3 | HOIPSs

We designed a slippery HOIPS with two regions of differing hydrophobicity to explore the possibility of controlling the movement direction of water droplets (Figure 3a). Regarding the formation of surfaces with two hydrophobicities, the design utilized the immiscibility between the fluorinated oil and other oils (Figure S9). The porous PTMSDPA and F-PTMSDPA films exhibited no notable structural changes, and fluorine was present only in the fluorinated regions (Figure S10). Driven by chemical affinity, the two compositionally heterogeneous oils selectively diffused and were stably fixed on their corresponding surfaces, remaining phase-separated because of immiscibility. Under UV illumination, the boundary between the two regions appeared more distinct (Figure S11). Whereas previous SLIPS systems typically required fluorescent dyes to distinguish lubricant domains, PTMSDPA's intrinsic fluorescence allows the two infused regions to be readily identified under UV light without any exogenous markers.

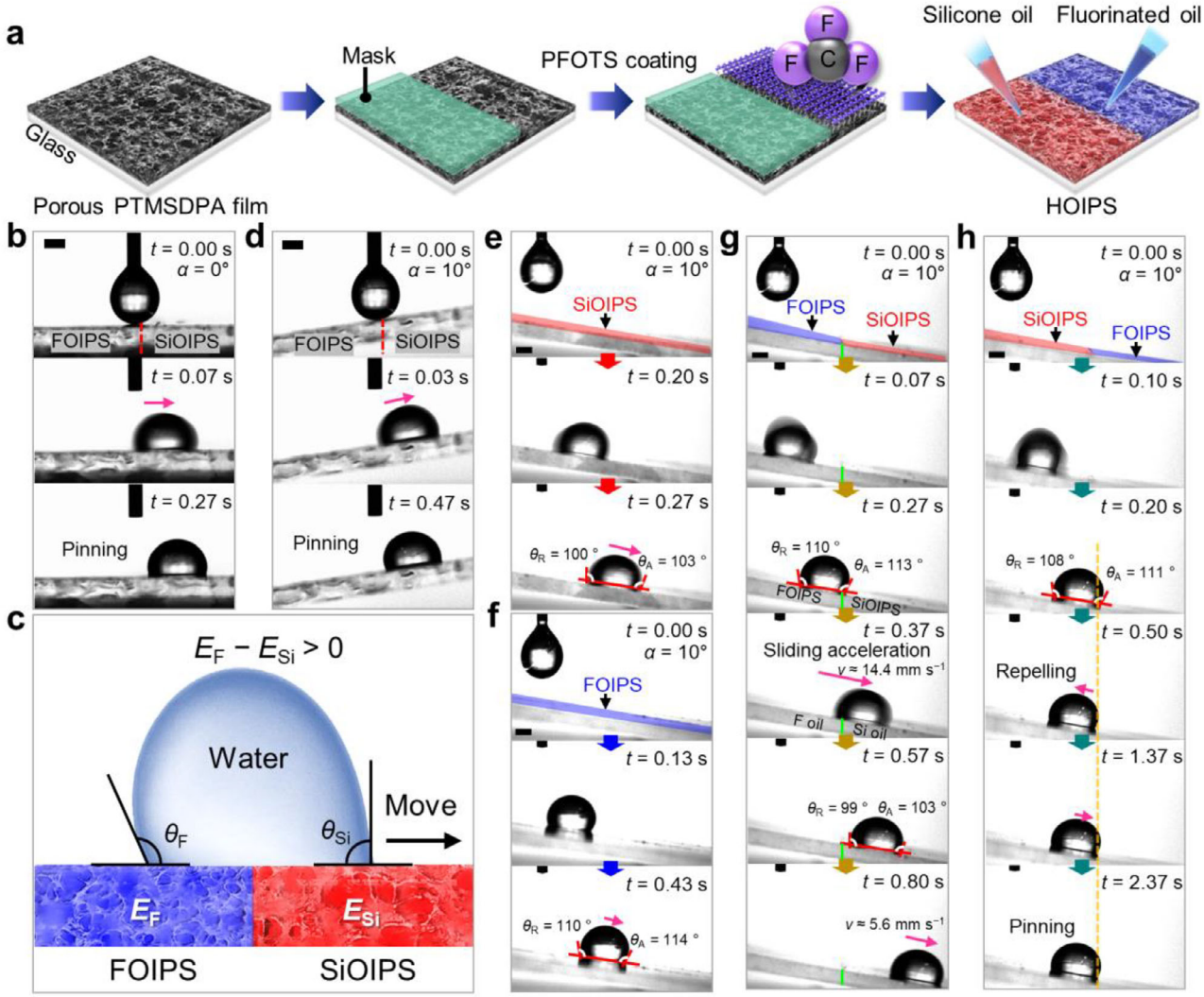

FIGURE 3 | (a) Schematic of slippery HOIPS fabrication. (b) Photographs illustrating the movement of a water droplet on the interface of slippery surfaces infused with fluorinated (FC-70) and silicone (Si 5 cSt) oils at $\alpha = 0°$. All scale bars equal 0.5 mm. (c) Schematic of directional droplet motion across the chemically patterned HOIPS interface. (d) Photographs illustrating droplet movement on the interface of slippery surfaces infused with FC-70 and Si 5 cSt oils at $\alpha = 10°$. All scale bars equal 5 mm. Photographs illustrating the movement of a water droplet on the (e) silicone-oil-infused porous surface (SiOIPS), (f) fluorinated-oil-infused porous surface (FOIPS), and (g,h) HOIPS (droplet moving (g) from the FOIPS to SiOIPS and (h) from the SiOIPS to FOIPS). θ_A and θ_R represent the advancing and receding contact angles, respectively. All scale bars equal 5 mm.

Figure 3b and Video S2 show water droplet movement on the HOIPS interface with an entirely level surface. Interestingly, the droplet on the HOIPS interface moved toward the silicone-oil-infused porous surface (SiOIPS). SiOIPSs, with their siloxane-based lubricant phases, are inherently hydrophobic and poorly wetted by water. However, despite their low polarity, they do not achieve the water repellency level of fluorinated-oil-infused porous surfaces (FOIPSs), which, owing to their fully fluorinated nonpolar nature, strongly repel aqueous droplets. This subtle difference in chemical interactions may promote the preferential migration of water droplets toward the silicone-oil-infused regions despite the minimal differences in the apparent wettability (Table S2).

Figure 3c illustrates directional droplet motion across a chemically patterned HOIPS interface under the condition of horizontal leveling. A droplet located at the interface between a FOIPS (more hydrophobic) and SiOIPS (less hydrophobic) migrates toward the more wettable region to minimize the interfacial energy. This energy-driven motion originates from the difference in the interfacial energy between the water droplet and the two SLIPSs (FOIPS and SiOIPS), enabling programmable droplet transport without reliance on surface topography or structural gradients.

Droplet behavior was further examined in the presence of excess silicone oil on the PTMSDPA surface. Although the height of the SiOIPS region exceeded that of the FOIPS region, the droplet migrated toward the former, which indicated that this movement was not driven by the height difference at the interface (Video S3). The droplet even climbed up the inclined surface despite the opposing force of gravity, i.e., the difference in hydrophobic repulsion overrode the gravitational effect (Figure 3d and Video S4).

To further explore droplet mobility control, we observed droplet movement on three different surfaces (SiOIPS, FOIPS, and

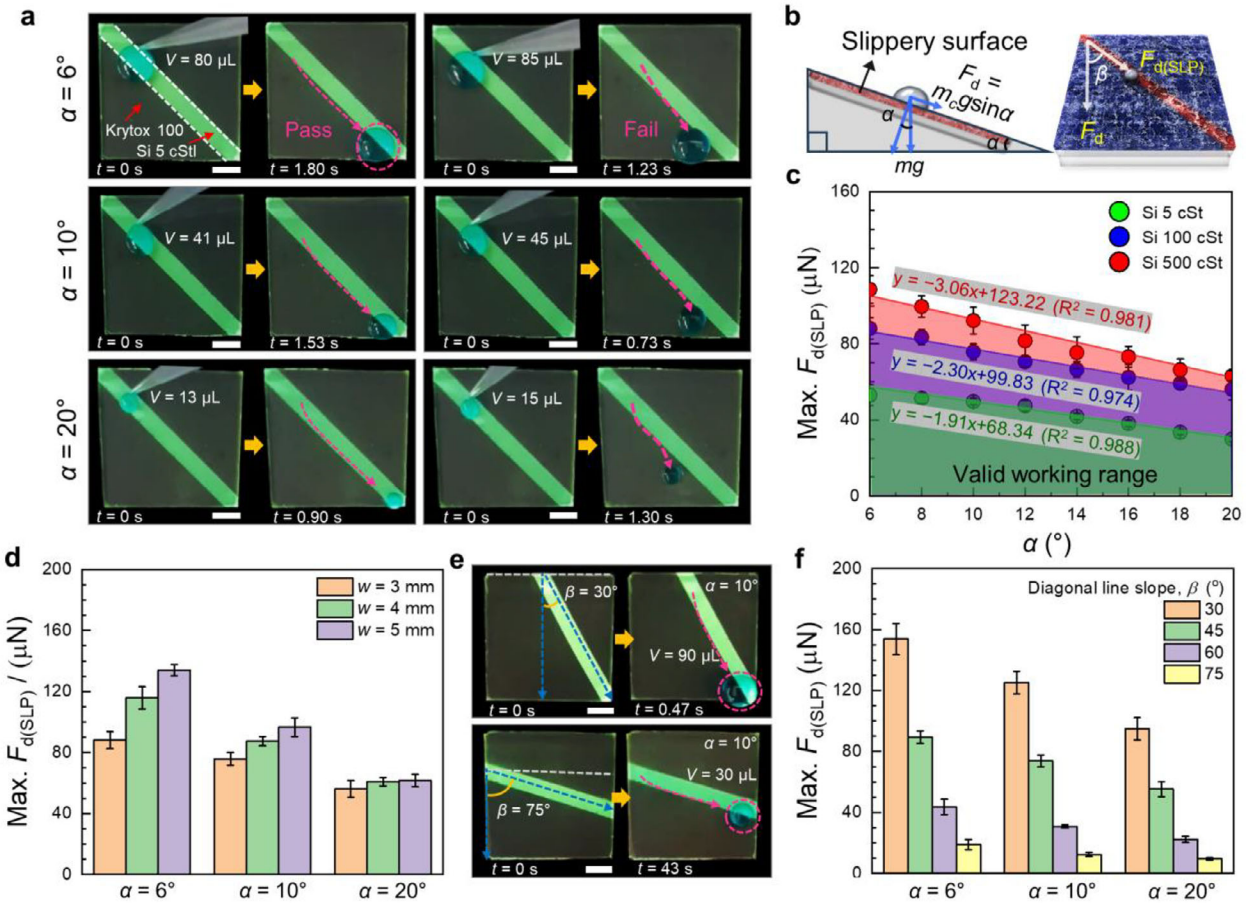

FIGURE 4 | (a) FL images illustrating the sliding behavior of water droplets with a specific volume on the HOIPS at $\alpha = 6°$, 10°, and 20° under UV light. The green diagonal line and other regions were infused with Si 5 cSt and Krytox 100 (fluorinated lubricant), respectively. All scale bars equal 5 mm. (b) Maximum downward force in the diagonal-line direction of the HOIPS (Max. $F_{d(SLP)}$). (c) Max. $F_{d(SLP)}$ as a function of α for three different HOIPSs consisting of the SiOIPS (region infused with Si 5, 100, or 500 cSt) and FOIPS (region infused with Krytox 100). (d) Max. $F_{d(SLP)}$ as a function of the width ($w = 3$, 4, 5 mm) of the diagonal line at $\alpha = 6°$, 10°, and 20°. (e) FL images illustrating the sliding behavior of water droplets on the HOIPS ($w = 3$ mm) with different droplet path angles of the diagonal line ($\beta = 30°$ and 75°) at $\alpha = 10°$ under UV light. All scale bars equal 5 mm. (f) Max. $F_{d(SLP)}$ depending on β (30°, 45°, 60°, and 75°) at $\alpha = 6°$, 10°, and 20°. In (d–f), the green diagonal line and other regions were infused with Si 100 cSt and Krytox 100, respectively. All Max. $F_{d(SLP)}$ are presented as means ± SDs ($n = 3$).

HOIPS) at $\alpha = 10°$. Both slippery surfaces (SiOIPS and FOIPS) exhibited excellent water sliding properties with low contact-angle hysteresis (<4°), defined as the difference between the advancing and receding contact angles (θ_A and θ_R, respectively) (Figure 3e,f). Sliding acceleration was observed when the water droplet transitioned from the fluorinated oil to the fluorinated–silicone oil interface, while the droplet sliding on the silicone oil was repelled and pinned instead of moving toward the fluorinated oil (Figure 3g,h, Video S5 and S6). Therefore, the designed HOIPS could enhance or restrict the movement of droplets depending on the surface hydrophobicity difference.

2.4 | Directional Movement of Water Droplets on the HOIPS

To investigate the directional movement of water droplets, we designed a HOIPS with a diagonal SiOIPS line surrounded by FOIPS regions (Figure S12). Figure 4a and Video S7 show the droplet sliding trajectories on the HOIPS (bright-green emission line: SiOIPS, surrounding regions: FOIPS; 365-nm UV light) for different α. As clearly shown in Figure 4a, the HOIPS surface exhibits distinct fluorescence contrast between the SiOIPS and FOIPS regions without the need for any external dye. This enables direct visualization of where each lubricant is infused and clearly delineates the path along which the water droplet is guided. The bright emission from the SiOIPS line under UV illumination serves not only as a functional channel for droplet transport but also as a built-in optical indicator of directional guidance.

The droplet moved along the SiOIPS line because the repulsive force exerted by the FOIPS overrode the gravitational effect, while departure from the path line was observed for droplets with masses above the critical mass. The droplet critical mass decreased with the increasing α owing to the concomitant increase in the sliding force. The maximum downward force capable of moving the droplet in the direction of the diagonal line on the HOIPS (Max. $F_{d(SLP)}$) can be defined as follows (Figure 4b and Equation (3)):

$$\text{Max. } F_{d(SLP)} = m_c\, g \sin\alpha \cos\beta \tag{3}$$

where m_c is the critical mass of a water droplet not deviating from the path line, g is the gravitational acceleration, and α and β are the tilting angle and droplet path angle of the diagonal line, respectively.

Figure 4c presents Max. $F_{d(SLP)}$ as a function of α for three different HOIPS configurations (the diagonal SiOIPS lines were infused with Si 5, 100, or 500 cSt, while the surrounding regions remained FOIPS). As the viscosity of the infused Si oils increased, m_c and Max. $F_{d(SLP)}$ increased for all tested α values (Figure 4c; Figures S13–S15). The use of higher-viscosity lubricants improved the robustness of the infused layer [41], which stabilized droplet motion and enabled the retention of larger droplets along the patterned surface. Within the limited α range investigated, the regression curves for all three HOIPSs were well approximated by linear functions, with slopes of −1.91, −2.30, and −3.06 for Si 5, 100, and 500 cSt, respectively, suggesting that the operational range of the system could be expanded by increasing silicone oil viscosity. This relationship provides a predictive framework for quantitatively estimating the maximum droplet volume and corresponding driving force relevant to droplet transport along a designated pathway within a given range of α.

To examine the relationship between the width of the diagonal line (w) and Max. $F_{d(SLP)}$, we prepared HOIPSs with $w = 3$, 4, and 5 mm. Figure 4d shows that at $\alpha = 20°$, Max. $F_{d(SLP)}$ remained within a similar range (56.1 ± 5.5 to 61.6 ± 4.1 μN). In contrast, at $\alpha = 6°$, a remarkable difference in Max. $F_{d(SLP)}$ was observed, with values of 88.1 ± 5.5, 115.9 ± 7.2, and 134.0 ± 3.6 μN observed for $w = 3$, 4, and 5 mm, respectively. The contact area of near-m_c droplets on the SiOIPS notably increased with the increasing w at $\alpha = 6°$ and 10°, whereas no notable variation was observed at $\alpha = 20°$ (Figure S16). These findings indicate that the increase in Max. $F_{d(SLP)}$ was influenced by the droplet–SiOIPS contact area.

The effect of the droplet path angle (β) of a diagonal line on the HOIPS was investigated at $\alpha = 10°$ (Figure 4e). The HOIPS with $\beta = 30°$ effectively directed the movement of a 90-μL droplet along the designed path. However, at $\beta = 75°$, only 30-μL droplets were successfully transported because of the stronger influence of gravity. As β increased from 30° to 75°, Max. $F_{d(SLP)}$ substantially decreased across all investigated α values, which highlights the importance of β as a key factor for controlling the directional movement of water droplets without deviation (Figure 4f; Figure S17). Compared with previously reported methodologies [14, 29], this approach enables the transport of droplets with a broader mass range over a wider range of diagonal slopes, thereby enhancing the controllability and applicability of droplet manipulation.

In addition to the geometric parameters governing droplet transport, the stability of the designed HOIPS (Figure 4a) was systematically evaluated (Figure S18). The α_c remained essentially unchanged over 10 days under ambient conditions, confirming the excellent durability of the lubricant-infused interface (Figure S18a). The SLIPS also exhibited strong chemical robustness when immersed in highly acidic (pH 1) and highly basic (pH 14) environments, showing only minimal variations in α_c even after extended exposure (Figure S18b). Furthermore, the surface maintained stable sliding behavior across a broad temperature range (20–90°C), demonstrating reliable thermal tolerance for practical operation under diverse environmental conditions (Figure S18c). These results collectively verify that the HOIPS architecture not only enables precise directional droplet manipulation but also maintains stable performance under various chemical and thermal conditions, thereby broadening its applicability in real-world droplet transport systems.

2.5 | Control of Droplet Movement on Designed HOIPS Forms

To explore the potential applications of HOIPSs for precise water droplet control, we examined the movement of droplets on HOIPS structures with various geometries. The droplets moved along the SiOIPS line of a right-angle bracket shape, which demonstrated that droplet movement can be effectively directed along curved paths by exploiting hydrophobicity differences (Figure 5a and Video S8). Moreover, the droplets placed at different starting positions migrated along predefined routes and ultimately converged at the designated endpoint (Figure 5b and Video S9).

The slippery surface (see the inset FL image in Figure 5c) could dynamically alter the movement route depending on the droplet volume under a downslope driving force of approximately 0.26 g (sin 15°) (Figure 5c and Video S10). The velocity of droplet movement and its overlapping area with the FOIPS surface were identified as critical factors determining the droplet trajectory at the crossroads (Figure S19). Small-volume droplets (5–7 μL) moved along the SiOIPS surface, maintaining their predefined directional paths. However, as the volume increased, the droplets slid along the SiOIPS–FOIPS interface because of the increased F_d, and the movement direction shifted to the initially contacted path at the intersection. The Max. $F_{d(SLP)}$ values of Paths A, B, and C for droplet-volume-sensitive separation were determined as 13.8 ± 3.3, 28.7 ± 8.1, and 51.7 ± 8.1 μN, respectively. These findings demonstrate that our system enables a unique mass-dependent routing mechanism, wherein heavier droplets follow pathways different from those observed for lighter droplets under the same HOIPS configuration. The observed volume-dependent droplet transport demonstrates that different mass thresholds can dynamically bias the direction of motion. This mechanism enables programmable, topography-free droplet routing, paving the way for the development of passive fluidic elements requiring no external actuation.

To evaluate the feasibility of controlling droplet movement on curved surfaces, we prepared a HOIPS with a central SiOIPS line on polyethylene terephthalate (thickness: 10 μm). A water droplet placed at the top of a curved flexible substrate (inverted U-shaped HOIPS) migrated downward along the SiOIPS path (Figure 5d and Video S11). In contrast, an inverted U-shaped SiOIPS structure failed to direct droplet movement, causing droplets to deviate from the intended path and fall off the surface. Furthermore, water droplets moved along the predefined pathways on a zigzag-patterned HOIPS coated onto a curved copper plate and rolled HOIPS film (Figure 5e,f and Video S12).

Droplet control strategies that rely on morphological surface features (e.g., grooves or micropatterns) may experience reduced robustness when applied to curved or deformable substrates, as such features can deform under compressive or tensile strain.

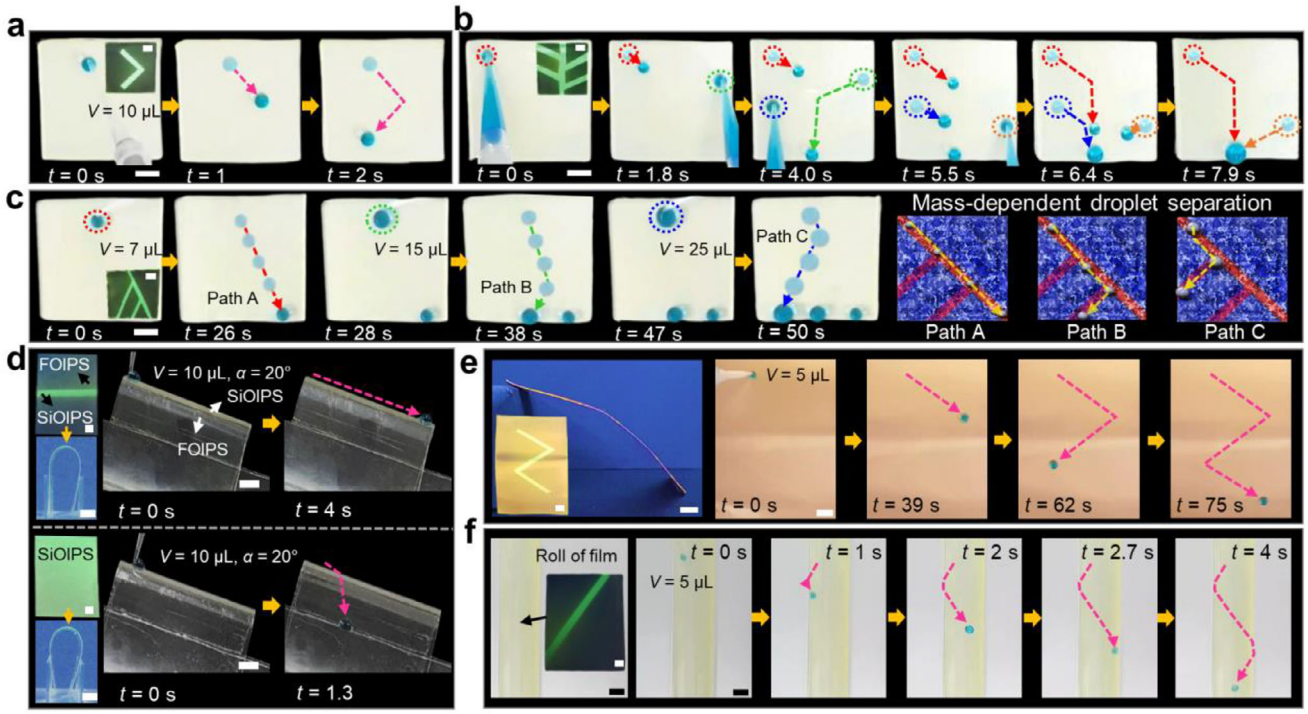

FIGURE 5 | Photographs of (a) migration direction change, (b) droplet merging, and (c) droplet-volume-sensitive separation on the fabricated HOIPS at $\alpha = 15°$. Insets represent the FL images used to identify specific HOIPS designs, such as (a) a right-angle bracket and (b,c) leaf-vein-like structures. Photographs of droplet movement on curved flexible surfaces: (d) inverted U-shaped HOIPS and SiOIPS and (e) zigzag line-shaped and (f) rolled HOIPS films. All scale bars equal 0.5 mm.

In this context, the ultrathin (~200 nm) and flexible nature of the polymer-based HOIPS demonstrated here enables conformal integration onto curved and deformable surfaces, while preserving the intended wettability contrast and droplet-guiding functionality. This demonstrates the potential of PTMSDPA-based slippery HOIPSs as tunable coating materials for the precise manipulation of water droplets on flat, flexible, and curved substrates without relying on physical confinement, topography, or asymmetric geometries.

2.6 | Water Condensation Test

Water-repellency durability is a critical requirement for the water condensation test, as repeated droplet impingement should not compromise the surface's liquid mobility. To evaluate the durability under cyclic droplet impact at a defined location, a HOIPS surface incorporating a 2-mm-wide SiOIPS line was fabricated. This design consideration was necessary because a 10-μL droplet spreads across multiple SiOIPS/FOIPS lines on sub-millimeter HOIPS patterns (0.5–1.0 mm), making it difficult to focus the influence of a single line on sliding behavior. For continuous droplet dispensing, the test was initiated at a sliding angle of 8°–10°, where droplets could avoid accumulation during the durability evaluation. As shown in Figure S20, the α remained consistently low (~10°) for the initial 40 cycles, indicating stable water-repellent performance. Although α gradually increased with further droplet impacts and reached approximately 15° after 100 cycles, the HOIPS surface still maintained a sufficiently low sliding angle, demonstrating excellent water-repellency durability suitable for water condensation applications.

To explore the possibility of exploiting the HOIPS morphology to efficiently condense water, HOIPS line patterns (HOIPS#1–#5, Table S3) with alternating SiOIPS and FOIPS regions were fabricated using an elastomeric shadow mask. The line widths of the HOIPS patterns, defined by combinations of SiOIPS (w_1) and FOIPS (w_2) were rationally selected to span a practical range (0.5–1.0 mm) and to investigate how binary hydrophobic contrast influences droplet coalescence, critical shedding diameter (CSD), defined here as the droplet diameter at the moment of gravitational detachment, and water collection behavior.

Figure 6a shows the time-lapse images of a droplet grown on HOIPS#1 ($w_1 = 0.75$ and $w_2 = 0.5$ mm). At the early stage (t = 385 s), water droplets condensed on the FOIPS region migrated toward the adjacent SiOIPS domain, driven by interfacial energy asymmetry, and subsequently coalesced with the growing droplet therein. Notably, the droplets in the SiOIPS regions exhibited a limited mobility because of the flanking FOIPS boundaries, which enhanced interactions with neighboring droplets and promoted their coalescence ($t = 388$ s). Consequently, the rapidly growing droplets (yellow circles) on the SiOIPS lines reached the CSD ($2r \approx 0.8$ mm) and were transported to the bottom of the slope because of gravity ($t = 416$ s).

This droplet migration and coalescence behavior was also observed for HOIPS#2 ($w_1 = 0.5$ and $w_2 = 0.75$ mm), in which case droplets originating from the FOIPS region coalesced within the SiOIPS domain to cause rapid initial growth. However, because the SiOIPS width was smaller than the typical CSD observed for SiOIPS (~0.7 mm), droplets of that size extended beyond the SiOIPS boundary. The adjacent FOIPS regions acted like invisible

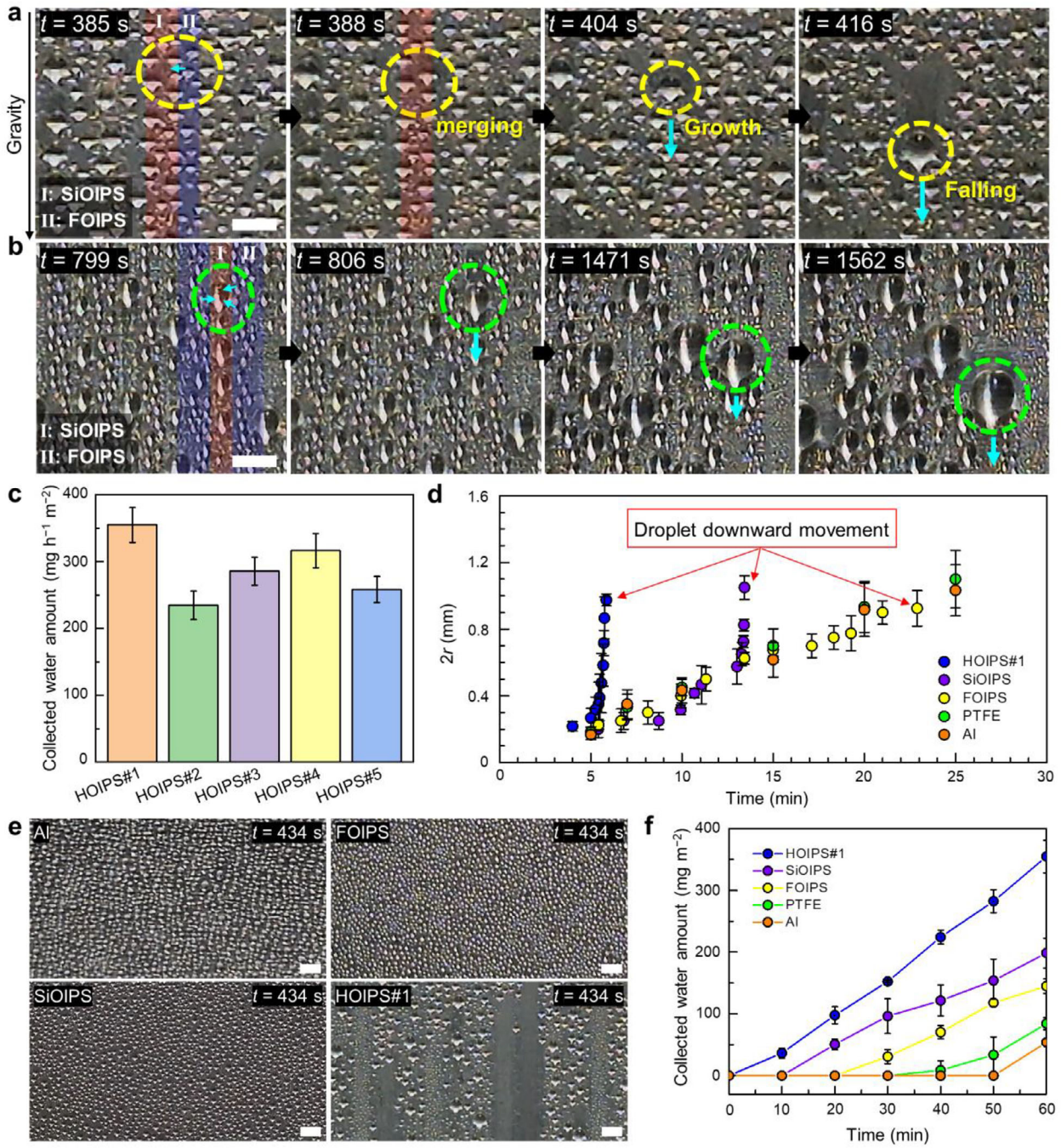

FIGURE 6 | Photographs of the condensed droplets formed on (a) HOIPS#1 and (b) HOIPS#2 at specific elapsed times. Red and blue stripes represent the alternately arranged SiOIPS and FOIPS regions, with the cyan arrows indicating the droplet movement direction. All scale bars equal 1 mm. (c) Amounts of water collected per unit area-hour on five different HOIPS patterns. (d) Time-dependent evolution of droplet radius during condensation on five different surfaces: Al, polytetrafluoroethylene, SiOIPS, FOIPS, and HOIPS#1. (e) Photographs of the condensed droplets formed on different surfaces at specific elapsed times. All scale bars equal 1 mm. (f) Collected water amount as a function of elapsed time on five different surfaces. All data are shown as means ± SDs ($n = 3$).

barriers, restricting downward movement and forcing droplets to grow heavier before detachment, which delayed their release compared with HOIPS#1 (Figure 6b).

The time-dependent evolution of droplet radius during condensation was examined on five distinct surface patterns, as shown in Figures S21 and S22. Droplets with CSD values of approximately 0.7–1.0 mm exhibited not only significantly faster but also nearly simultaneous downward motion on HOIPS#1, #3, and #4, all of which featured sufficiently wide SiOIPS regions ($w_1 \geq 0.75$ mm) to support efficient droplet departure. In contrast, the w_1 of HOIPS#2 was relatively narrow, resulting in a significantly longer retention time before droplets reached the CSD. These observations suggest that the downward movement of condensed droplets is highly dependent on the lateral width of the SiOIPS region; a minimum width of approximately 0.7 mm

is sufficient to overcome confinement and trigger synchronized droplet removal during condensation-driven growth. Controlling the droplet release time plays a critical role in increasing the net water yield by minimizing evaporation losses during condensation [42]. This becomes particularly important under high solar irradiance or low relative humidity conditions [43]. These findings indicate that our system allows programmable control of droplet departure time through simple pattern adjustments, enabling practical optimization of water harvesting performance under diverse environmental conditions.

Figure 6c quantifies the water collection per unit area-hour for five HOIPS configurations. HOIPS#1 exhibited the highest collection rate (354.8 ± 26.2 mg h^{-1} m^{-2}) at w_1 = 0.75 mm and w_2 = 0.5 mm (w_1/w_2 = 1.5). The overall water collection followed the order HOIPS#1 > HOIPS#4 > HOIPS#3 > HOIPS#5 > HOIPS#2, which appears to qualitatively track this ratio sequence (1.5, 1.33, 1.0, 0.75, 0.67). While the number of tested configurations is limited, this trend suggests that a larger w_1/w_2 ratio may promote higher harvesting efficiency. Consistent with this, the onset of downward droplet motion was similar for HOIPS#1, #3, and #4, followed by HOIPS#2, with HOIPS#5 showing the latest release (Figure S21). Narrower FOIPS spacing may facilitate more frequent droplet transfer and coalescence, whereas wider SiOIPS domains support stable directional sliding and efficient shedding. These findings highlight the potential of using simple geometric ratios to tune HOIPS performance for specific water harvesting requirements.

A quantitative analysis of droplet growth behavior on various surfaces was conducted by plotting the time-dependent evolution of droplet diameter (Figure 6d). Although the SiOIPS initially exhibited a growth trajectory comparable with those of Al and polytetrafluoroethylene (PTFE) surfaces, a pronounced increase in droplet size occurred at ~781 s because of coalescence with neighboring droplets, resulting in a rapid transition to downward motion. In contrast, FOIPS maintained a linear growth profile and reached the CSD considerably later (t = 1374 s) than SiOIPS.

On the HOIPS structure, droplet growth was markedly accelerated at ~330 s, initiated by directional migration toward the SiOIPS region driven by interfacial energy asymmetry. The chemically imposed confinement in the SiOIPS domain facilitated the merging of surrounding droplets, enabling rapid CSD attainment. The CSD values of HOIPS were 0.72 ± 0.08 mm, which were significantly smaller than those of other control surfaces, such as SiOIPS (0.88 ± 0.04 mm), FOIPS (0.93 ± 0.11 mm), PTFE (2.60 ± 0.53 mm), and Al (2.85 ± 0.21 mm). Notably, the reduced CSD of HOIPS is comparable to the SiOIPS stripe width (w_1 = 0.75 mm). Therefore, once a droplet reaches a diameter close to w_1, the interaction the surface-energy contrast between the SiOIPS stripe and the neighboring FOIPS regions imposes a geometry-driven depinning instability, allowing detachment at a much smaller size. This boundary-mediated destabilization significantly accelerates droplet turnover and ultimately enhances water collection efficiency.

Figure 6e shows the images of condensed water droplets on four different surfaces (Al, FOIPS, SiOIPS, and HOIPS#1) at an identical elapsed time. Water droplets on the Al, FOIPS, and SiOIPS surfaces remained stationary even after 434 s, whereas those on the HOIPS#1 surface were transported to the bottom of the slope because of accelerated droplet growth. Compared with SiOIPS, which exhibited the highest droplet transport rate among the control surfaces, HOIPS#1 demonstrated a superior performance indicating that the alternating SiOIPS–FOIPS array with optimized line widths markedly enhanced water turnover by promoting droplet growth and gravity-assisted transport (Video S13).

The amounts of collected water over time were measured for five different surfaces to evaluate their water collection efficiencies (Figure 6f). The water collection efficiency of HOIPS#1 (354.8 ± 26.2 mg h^{-1} m^{-2}) was 1.8, 2.5, and 4.2 times higher than those of the SiOIPS (198.5 ± 24.2 mg h^{-1} m^{-2}), FOIPS (144.8 ± 12.0 mg h^{-1} m^{-2}), and PTFE sheet (53.9 ± 5.8 mg h^{-1} m^{-2}), respectively. All patterned surfaces exhibited meaningfully higher amounts of collected water compared to the other control surfaces (Figure S23). Notably, despite using less than half the amount of fluorinated lubricant compared to fully infused FOIPS films, the patterned HOIPS surfaces achieved superior water collection performance (up to 2.5 × higher). This highlights the effectiveness of our dual-lubricant patterning strategy not only in enhancing harvesting efficiency, but also in reducing fluorinated oil usage—offering a more sustainable and material-efficient approach for practical water harvesting applications.

In addition to this material efficiency, our HOIPS design also demonstrates a high level of performance compared with previously reported engineered SLIPSs. Although absolute comparisons are limited by the variations in the control SLIPS definitions and experimental conditions across studies, our HOIPS design exhibits a high water collection efficiency compared with previously reported engineered SLIPSs (Table S4). Therefore, these engineered slippery surface patterns, featuring an alternating infusion of two oils with distinct hydrophobicities, hold promise for water harvesting applications because of their enhanced droplet growth and high water turnover efficiency.

3 | Conclusion

We have developed a scalable, topography-free SLIPS (slippery liquid-infused porous surface) platform based on chemically patterned PTMSDPA films infused with dual lubricants, enabling programmable droplet transport. The formation of distinct lubricant domains within the porous PTMSDPA matrix is achieved through regional fluorination followed by sequential lubricant infusion, which establishes controlled interfacial energy asymmetry responsible for droplet routing. The HOIPS not only enables real-time, fluorescence-based visualization of two infused lubricant domains without exogenous markers and clearly delineates droplet-guiding pathways, but also allows directional control of droplet motion on flexible and curved substrates.

Combinations of SiOIPS and FOIPS line widths provide a transferable framework for engineering droplet behavior, including droplet coalescence, shedding diameter, and release timing during condensation, across diverse SLIPS-based systems. This design strategy offers a route to increasing net water yield under varied ambient conditions. Crucially, optimized HOIPS

line patterns achieve approximately 2.5 × higher water-harvesting efficiency compared to fluorinated-oil-based SLIPS.

Taken together, our study establishes a versatile SLIPS system for logic-based droplet routing, high-efficiency water harvesting, and adaptive fluidic manipulation. Ongoing studies are investigating the mechanical durability of these ultrathin films under dynamic fluidic impacts, aiming to validate their long-term stability and expand applicability to real-world operating conditions across environmental, biomedical, and energy-related applications.

4 | Experimental Section

4.1 | Materials

4-(Trimethylsilyl)diphenylacetylene (TMSDPA) was purchased from Alfa Aesar (Ward Hill, MA, USA). Tetrabutyltin was obtained from Tokyo Chemical Industry (Tokyo, Japan). $TaCl_5$ and toluene were acquired from Sigma–Aldrich (Saint Louis, MO, USA). Silicone oils based on PDMS with kinematic viscosities of 5, 100, and 500 cSt at 25°C (denoted as Si 5, 100, and 500 cSt, respectively) and PPMS oils, namely AP100 (viscosity ≈ 93.5–94.3 cSt at 25°C), AP1000 (viscosity ≈ 917 cSt at 25°C), and AR (viscosity = 450–550 cSt at 25°C), were obtained from Sigma–Aldrich Co. Krytox 100 (perfluorinated polyether) was purchased from DuPont Co. (Wilmington, DE, USA). Paraffin oil, jojoba oil (from *Simmondsia chinensis*), and FC-70 were provided by Sigma–Aldrich Co. Mineral oil (N100; viscosity = 246.1 cSt at 25°C) was procured from Cannon Instrument Co. (State College, PA, USA). PFOTS (97%), PS (weight-average molecular weight (M_w) = 192,000 g mol^{-1}), and MEK were obtained from Sigma–Aldrich Co. Methanol (99.8%) was purchased from Duksan (Gyeonggi-do, Republic of Korea). Acetone (99.5%) and ethanol (99.9%) were obtained from Samchun Pure Chemical Co. (Gyeonggi, Republic of Korea). All chemicals were used without further purification.

4.2 | Synthesis of PTMSDPA

PTMSDPA was prepared as described elsewhere (Figure S24) [44], with its M_w and polydispersity index determined as ~1,180,000 g mol^{-1} and 6.04, respectively (Figure S25). In a glove box with a nitrogen atmosphere, TMSDPA (5 mmol, 1.25 g) was placed in a 10 mL vial and dissolved in toluene (5 mL). The catalyst solution was prepared by dissolving $TaCl_5$ (0.2 mmol, 0.07 g) and tetrabutyltin (0.4 mmol, 0.14 g) in toluene (4.9 mL) in a Schlenk tube. The catalyst solution was preactivated at 80°C for 10 min and then supplemented with the monomer solution. The mixture was stirred at 80°C for 24 h, cooled to room temperature, diluted with toluene (100 mL), and poured into methanol. The resulting precipitate was isolated by filtration to obtain PTMSDPA as orange threads (~1.0 g, yield: ~80%).

4.3 | Fabrication of Porous PTMSDPA Thin Films

Porous PTMSDPA thin films were fabricated using a typical spin-coating method and selective solvent extraction. Glass substrates (2.5 cm × 2.5 cm × 1 mm) were cleaned by sequential ultrasonication in acetone, ethanol, and distilled water (5 min each) and blown dry with nitrogen gas. PTMSDPA and PS were separately dissolved in toluene at 1 wt.%, and the solutions were mixed at seven different ratios (PTMSDPA:PS = 0.1:0.9, 0.2:0.8, …, 0.7:0.3 wt.%/wt.%). The desired mixture (500 µL) was dropped onto the cleaned substrate and spin-coated at 1000 rpm for 1 min. PS, the sacrificial polymer used to create the porous structure of the PTMSDPA thin films, was removed by immersing the PTMSDPA/PS blend films into MEK for 40 min. Planar PTMSDPA films with a thickness of 92 ± 10 nm (Figure S26) were fabricated by spin-coating under the above-mentioned conditions using a 0.4 wt.% solution of PTMSDPA in toluene.

4.4 | Preparation of Slippery HOIPSs

A portion of the porous PTMSDPA film surface was covered with an elastomer mask (Sylgard 184 PDMS, Dow Corning Co., Auburn Hills, MI, USA) of a specific size and shape. The exposed surface was activated using O_2 plasma treatment (Solarus 950, Gatan Inc., CA, USA) for 3 min. PFOTS (7 µL) was placed into a plastic Petri dish containing the plasma-treated sample, the dish was sealed, and vapor phase deposition was performed at 60°C for 40 min [45, 46]. The sample was carefully separated from the mask and rinsed several times with ethanol. To prepare the slippery surfaces, silicone oil was initially applied to the entire film. Owing to its chemical affinity, the oil preferentially wetted and remained within the PTMSDPA regions. Subsequently, the fluorinated oil was infused into the remaining F-PTMSDPA regions, and the excess oil was removed by spin-coating at 1000 rpm for 1 min.

4.5 | Characterization

FL emission spectra were recorded using an FL spectrometer (LS-55, PerkinElmer Inc., Waltham, MA, USA, NFEC-2019-02-254215) for PTMSDPA films coated on glass slides and infused with different oils. All FL spectra were recorded using an excitation wavelength of 420 nm and excitation/emission slit widths of 10 nm. FT-IR spectroscopy in attenuated total reflectance mode (Nicolet 5700, Thermo Fisher Scientific Inc., Waltham, MA, USA, NFEC-2007-10-011098) was used to analyze the chemical composition of freestanding film samples. FT-IR spectra were acquired in the range of 4000–400 cm^{-1} at a resolution of 4 cm^{-1} by averaging 32 scans per sample. Background spectra were collected in air, and no additional spectral corrections were applied. Tapping-mode atomic force microscopy (Dimension Icon, Bruker Inc., Manning Road Billerica, MA, USA, NFEC-2022-02-276624) was used to determine the roughness ratios of the porous PTMSDPA film. Measurements were performed over an area of 10 µm × 5 µm under ambient conditions. Plane-leveling was applied using the Roller function in the Nanoscope software to account for the background tilt and curvature. The surface morphologies of the porous PTMSDPA and F-PTMSDPA films were characterized using an FE-SEM instrument (GeminiSEM 560, Carl Zeiss Co. Ltd., Oberkochen, Germany, NFEC-2022-08-280820) equipped with SE2 and In-Lens detectors. The PTMSDPA-coated glass substrates were cut into 1-cm^2 pieces and subsequently coated with Pt by sputtering for 2 min. All measurements were performed at an accelerating voltage of 5 kV.

The distribution of fluorine atoms on the partially fluorinated porous polymer surface was analyzed using FE-SEM coupled with energy-dispersive X-ray spectroscopy (XFlash Detector 5030, Bruker Inc.) at an accelerating voltage of 10 kV. The contact angles of water and various oils on flat PTMSDPA surfaces, along with their surface and interfacial tensions, were measured using a contact angle meter (Phoenix 300-O, SEO Corp., Gyeonggi-do, Republic of Korea). Droplets were dispensed by using 22-gauge needles. Contact angle measurements were performed three times, and surface/interfacial tension measurements were conducted 10 times. All measurements were carried out under ambient conditions at 24 ± 1 °C and a relative humidity of 45–55%. The sliding behavior of water droplets was tested three times using a precision tilt stage (STX-40-15, Science Town Co., Ltd., Incheon, Republic of Korea). The sliding behavior of water droplets on the SLIPSs was documented using photo and video recordings using a digital camera equipped with a Sony IMX754 periscope-style telephoto lens (10 MP, 240 mm equivalent focal length). As shown Figure S27, condensation experiments were performed under ambient laboratory conditions (temperature: 24 ± 1°C, relative humidity: 55 ± 5%) with humidity regulated using a dehumidifier (NED-280, Nawooel Co., Gyeonggi, Republic of Korea). The saturation vapor pressure at 24 °C was approximately 2.98 kPa, based on standard psychrometric data. The experiments were conducted in the presence of non-condensable gases naturally present in air, such as nitrogen and oxygen. A Peltier thermoelectric module (20 mm × 20 × mm × 3.5 mm, TEC1-04904, China) mounted on a cooling pan plate (40 mm, CN5, Zhanpeng Electronic Technology Co., Ltd., Beijing, China) was vertically fixed on a bracket and connected to a direct-current power supply (LUZ3010C, Zhongshan Jiachen Optoelectronics Technology Co., Ltd., Guangdong, China). The test sample was placed on the Peltier cooling plate, and the substrate surface temperature was maintained at 7 ± 1 °C for all condensation experiments by applying a voltage of 5 V. The temperature was measured using an LCD digital thermometer (Lap & Tools, Seoul, Republic of Korea). The weight of water collected at different elapsed times was measured using an analytical balance (Mettler Toledo ML54, Mettler-Toledo Inc., Columbus, OH, USA). All SLIPS samples were fabricated on commercially available Al substrates (OON brand, OEM product, China) with a thickness of 0.2 mm. The experimental setup was designed and implemented with reference to previous studies [16, 17].

Author Contributions

J.Y. and W.-E.L. conceived the idea. J.Y., G.K., and W.-E.L. designed the experiments. J.Y., E.K., and J.L. performed the experiments. D.Y.C. conducted the visualization. J.Y., J.H.K., H.Y., J.L., K.H., G.K., Y.-J.J., and W.-E.L. analyzed the data. J.H.K. performed the physical modeling of droplet transport. J.Y., G. K., and W.-E. L. wrote the manuscript. All authors discussed the results and commented on the manuscript.

Conflicts of Interest

The authors declare no conflict of interest.

Data Availability Statement

All data supporting the findings of this study are contained within the article and Supplementary Information.

References

1. X. Yao, Y. Song, and L. Jiang, "Applications of Bio-Inspired Special Wettable Surfaces," *Advanced Materials* 23 (2011): 719–734, https://doi.org/10.1002/adma.201002689.

2. W. Barthlott and C. Neinhuis, "Purity of the Sacred Lotus, or Escape from Contamination in Biological Surfaces," *Planta* 202 (1997): 1–8, https://doi.org/10.1007/s004250050096.

3. A. Tuteja, W. Choi, M. Ma, et al., "Designing Superoleophobic Surfaces," *Science* 318 (2007): 1618–1622, https://doi.org/10.1126/science.1148326.

4. C. Frankiewicz and D. Attinger, "Texture and Wettability of Metallic Lotus Leaves," *Nanoscale* 8 (2016): 3982–3990, https://doi.org/10.1039/C5NR04098A.

5. G. D. Bixler and B. Bhushan, "Bioinspired Rice Leaf and Butterfly Wing Surface Structures Combining Shark Skin and Lotus Effects," *Soft Matter* 8 (2012): 11271–11284, https://doi.org/10.1039/c2sm26655e.

6. T.-S. Wong, S. H. Kang, S. K. Y. Tang, et al., "Bioinspired Self-Repairing Slippery Surfaces With Pressure-Stable Omniphobicity," *Nature* 477 (2011): 443–447, https://doi.org/10.1038/nature10447.

7. S. Sunny, N. Vogel, C. Howell, T. L. Vu, and J. Aizenberg, "Lubricant-Infused Nanoparticulate Coatings Assembled by Layer-by-Layer Deposition," *Advanced Functional Materials* 24 (2014): 6658–6667, https://doi.org/10.1002/adfm.201401289.

8. X. Tian, S. Banerjee, I. Gonzalez-Alfonzo, and L. Cademartiri, "Suppressing Evaporative Loss in Slippery Liquid-Infused Porous Surfaces (SLIPS) With Self-Suspended Perfluorinated Nanoparticles," *Langmuir* 36 (2020): 5106–5111, https://doi.org/10.1021/acs.langmuir.0c00160.

9. C. Long, Y. Qing, K. An, et al., "Functional Fluorination Agents for Opposite Extreme Wettability Coatings With Robustness, Water Splash Inhibition, and Controllable Oil Transport," *Chemical Engineering Journal* 415 (2021): 128895, https://doi.org/10.1016/j.cej.2021.128895.

10. J. Liu, Y. Sun X Zhou, X. Li, M. Kappl, W. Steffen, and H.-J. Butt, "One-Step Synthesis of a Durable and Liquid-Repellent Poly(dimethylsiloxane) Coating," *Advanced Materials* 33 (2021): 2100237, https://doi.org/10.1002/adma.202100237.

11. D. Parbat, A. Z. Hameed, Y. Kim, et al., "PDMS-Brush Modified Dual-Phase Lubricant-Infused Slippery Oleogel for Sustainable Shear Resistance," *Chemical Engineering Journal* 496 (2024): 153557, https://doi.org/10.1016/j.cej.2024.153557.

12. X. Yao, S. Wu, L. Chen, et al., "Self-Replenishable Anti-Waxing Organogel Materials," *Angewandte Chemie International Edition* 54 (2015): 8975–8979, https://doi.org/10.1002/anie.201503031.

13. T.-L. Chen, Y.-P. Lin, C.-H. Chien, et al., "Fabrication of Frog-Skin-Inspired Slippery Antibiofouling Coatings Through Degradable Block Copolymer Wrinkling," *Advanced Functional Materials* 31 (2021): 2104173, https://doi.org/10.1002/adfm.202104173.

14. U. Manna and D. M. Lynn, "Fabrication of Liquid-Infused Surfaces Using Reactive Polymer Multilayers: Principles for Manipulating the Behaviors and Mobilities of Aqueous Fluids on Slippery Liquid Interfaces," *Advanced Materials* 27 (2015): 3007–3012, https://doi.org/10.1002/adma.201500893.

15. J. Ma, W. Pan, Y. Li, and J. Song, "Slippery Coating Without Loss of Lubricant," *Chemical Engineering Journal* 444 (2022): 136606, https://doi.org/10.1016/j.cej.2022.136606.

16. K.-C. Park, P. Kim, A. Grinthal, N. He, D. Fox, and J. C. Weaver, "Condensation on Slippery Asymmetric Bumps," *Nature* 531 (2016): 78–82, https://doi.org/10.1038/nature16956.

17. B. Qi, X. Yang, and X. Wang, "Ultraslippery/hydrophilic Patterned Surfaces for Efficient Fog Harvest," *Colloids and Surfaces A: Physicochemical and Engineering Aspects* 640 (2022): 128398, https://doi.org/10.1016/j.colsurfa.2022.128398.

18. H. Luo, Y. Lu, S. Yin, et al., "Robust Platform for Water Harvesting and Directional Transport," *Journal of Materials Chemistry A* 6 (2018): 5635–5643, https://doi.org/10.1039/C8TA01096J.

19. X. Dai, N. Sun, S. O. Nielsen, et al., "Hydrophilic Directional Slippery Rough Surfaces for Water Harvesting," *Science Advances* 4 (2018): aaq0919, https://doi.org/10.1126/sciadv.aaq0919.

20. K. Maji, A. Das, M. Dhar, and U. Manna, "Synergistic Chemical Patterns on a Hydrophilic Slippery Liquid Infused Porous Surface (SLIPS) for Water Harvesting Applications," *Journal of Materials Chemistry A* 8 (2020): 25040–25046, https://doi.org/10.1039/D0TA09271A.

21. R. Feng, C. Xu, F. Song, F. Wang, X.-L. Wang, and Y.-Z. Wang, "A Bioinspired Slippery Surface With Stable Lubricant Impregnation for Efficient Water Harvesting," *ACS Applied Materials & Interfaces* 12 (2020): 12373–12381, https://doi.org/10.1021/acsami.0c00234.

22. N. Kalyani, M. C. Pastor, L. Pezzarossa, et al., "Antifouling Slippery Liquid Infused Porous Surface for Surfactant-Free PCR on Digital Microfluidics Platform," *Talanta* 282 (2025): 127001, https://doi.org/10.1016/j.talanta.2024.127001.

23. I. You, T. G. Lee, Y. S. Nam, and H. Lee, "Fabrication of a Micro-Omnifluidic Device by Omniphilic/Omniphobic Patterning on Nanostructured Surfaces," *ACS Nano* 8 (2014): 9016–9024, https://doi.org/10.1021/nn502226v.

24. S. Ling, Y. Luo, L. Luan, Z. Wang, and T. Wu, "Inkjet Printing of Patterned Ultra-Slippery Surfaces for Planar Droplet Manipulation," *Sensors and Actuators B: Chemical* 235 (2016): 732–738, https://doi.org/10.1016/j.snb.2016.06.120.

25. Q. Li, D. Wu, and Z. Guo, "Drop/Bubble Transportation and Controllable Manipulation on Patterned Slippery Lubricant Infused Surfaces With Tunable Wettability," *Soft Matter* 15 (2019): 6803–6810, https://doi.org/10.1039/C9SM01167F.

26. W. P. Huang, X. Chen, M. Hu, et al., "Patterned Slippery Surface Through Dynamically Controlling Surface Structures for Droplet Microarray," *Chemistry of Materials* 31 (2019): 834–841, https://doi.org/10.1021/acs.chemmater.8b03957.

27. C. Zhang, B. Zhang, H. Ma, et al., "Bioinspired Pressure-Tolerant Asymmetric Slippery Surface for Continuous Self-Transport of Gas Bubbles in Aqueous Environment," *ACS Nano* 12 (2018): 2048–2055, https://doi.org/10.1021/acsnano.8b00192.

28. X. Yang, K. Zhuang, Y. Lu, and X. Wang, "Creation of Topological Ultraslippery Surfaces for Droplet Motion Control," *ACS Nano* 15 (2020): 2589–2599, https://doi.org/10.1021/acsnano.0c07417.

29. J. Kamei and H. Yabu, "On-Demand Liquid Transportation Using Bioinspired Omniphobic Lubricated Surfaces Based on Self-Organized Honeycomb and Pincushion Films," *Advanced Functional Materials* 25 (2015): 4195–4201, https://doi.org/10.1002/adfm.201501020.

30. M. S. Sadullah, G. Launay, J. Parle, et al., "Bidirectional Motion of Droplets on Gradient Liquid Infused Surfaces," *Communications Physics* 3 (2020): 166, https://doi.org/10.1038/s42005-020-00429-8.

31. M. Sharma, S. Gupta, B. Bhatt, G. Bhatt, S. Bhattacharya, and K. Khare, "Anisotropic Motion of Aqueous Drops on Lubricated Chemically Heterogenous Slippery Surfaces," *Advanced Materials Interfaces* 8 (2021): 2001916, https://doi.org/10.1002/admi.202001916.

32. M. Pelizzari, G. McHale, S. Armstrong, et al., "Droplet Self-Propulsion on Slippery Liquid-Infused Surfaces With Dual-Lubricant Wedge-Shaped Wettability Patterns," *Langmuir* 39 (2023): 15676–15689, https://doi.org/10.1021/acs.langmuir.3c02205.

33. D. Paulssen, S. Hardt, and P. A. Levkin, "Droplet Sorting and Manipulation on Patterned Two-Phase Slippery Lubricant-Infused Surface," *ACS Applied Materials & Interfaces* 11 (2019): 16130–16138, https://doi.org/10.1021/acsami.8b21879.

34. W.-E. Lee, C.-L. Lee, T. Sakaguchi, M. Fujiki, and G. Kwak, "Fluorescent Viscosity Sensor Film of Molecular-Scale Porous Polymer With Intramolecular π-Stack Structure," *Macromolecules* 44 (2011): 432–436, https://doi.org/10.1021/ma102798j.

35. G. Kwak, W.-E. Lee, H. Jeong, T. Sakaguchi, and M. Fujiki, "Swelling-Induced Emission Enhancement in Substituted Acetylene Polymer Film With Large Fractional Free Volume: Fluorescence Response to Organic Solvent Stimuli," *Macromolecules* 42 (2009): 20–24, https://doi.org/10.1021/ma802506x.

36. D. Daniel, J. V. I. Timonen, R. Li, S. J. Velling, and J. Aizenberg, "Oleoplaning Droplets on Lubricated Surfaces," *Nature Physics* 13 (2017): 1020–1025, https://doi.org/10.1038/nphys4177.

37. N. Vogel, R. A. Belisle, B. Hatton, T.-S. Wong, and J. Aizenberg, "Transparency and Damage Tolerance of Patternable Omniphobic Lubricated Surfaces Based on Inverse Colloidal Monolayers," *Nature Communications* 4 (2013): 2176, https://doi.org/10.1038/ncomms3176.

38. T. Shen, M. Chen, H. Zhang, J. Z. Sun, and B. Z. Tang, "Copolymers of 4-Trimethylsilyl Diphenyl Acetylene and 1-Trimethylsilyl-1-Propyne: Polymer Synthesis and Luminescent Property Adjustment," *Molecules* 28 (2022): 27, https://doi.org/10.3390/molecules28010027.

39. I. Soga and S. Granick, "Infrared Dichroism and Surface Conformational Dynamics of Adsorbed Poly(dimethylsiloxane)," *Macromolecules* 31 (1998): 5450–5455, https://doi.org/10.1021/ma961416t.

40. D. Cao, X. Sun, H. Gao, L. Pan, N. Li, and Y. Li, "Crosslinked Polynorbornene-Based Anion Exchange Membranes With Perfluorinated Branch Chains," *Polymers* 15 (2023): 1073, https://doi.org/10.3390/polym15051073.

41. L. O. Prieto-López, P. Herbeck-Engel, L. Yang, Q. Wu, J. Li, and J. Cui, "When Ultimate Adhesive Mechanism Meets Ultimate Anti-Fouling Surfaces—Polydopamine Versus SLIPS: Which One Prevails?," *Advanced Materials Interfaces* 7 (2020): 2000876, https://doi.org/10.1002/admi.202000876.

42. K.-C. Park, S. S. Chhatre, S. Srinivasan, R. E. Cohen, and G. H. McKinley, "Optimal Design of Permeable Fiber Network Structures for Fog Harvesting," *Langmuir* 29 (2013): 13269–13277, https://doi.org/10.1021/la402409f.

43. O. Klemm, R. S. Schemenauer, A. Lummerich, et al., "Fog as a Fresh-Water Resource: Overview and Perspectives," *Ambio* 41 (2012): 221–234, https://doi.org/10.1007/s13280-012-0247-8.

44. T. Sakaguchi, K. Yumoto, M. Shiotsuki, F. Sanda, M. Yoshikawa, and T. Masuda, "Synthesis of Poly(diphenylacetylene) Membranes by Desilylation of Various Precursor Polymers and Their Properties," *Macromolecules* 38 (2005): 2704–2709, https://doi.org/10.1021/ma047632g.

45. J. C. Yang, J. Lee, S. J. Lim, G. Kwak, and J. Park, "Molecularly Imprinted Chalcone-Branched Polyimide-Based Chemosensors With Stripe Nanopatterns for the Detection of Melittin," *ACS Sensors* 8 (2023): 2298–2308, https://doi.org/10.1021/acssensors.3c00341.

46. D. Myung, S. Hussain, and S.-Y. Park, "Photonic Calcium and Humidity Array Sensor Prepared With Reactive Cholesteric Liquid Crystal Mesogens," *Sensors and Actuators B: Chemical* 298 (2019): 126894, https://doi.org/10.1016/j.snb.2019.126894.

Supporting Information

Additional supporting information can be found online in the Supporting Information section.

Supporting File: smll72674-sup-0001-SuppMat.docx